J. Fluid Mech. (2024), *vol*. 998, A29, doi:10.1017/jfm.2024.906

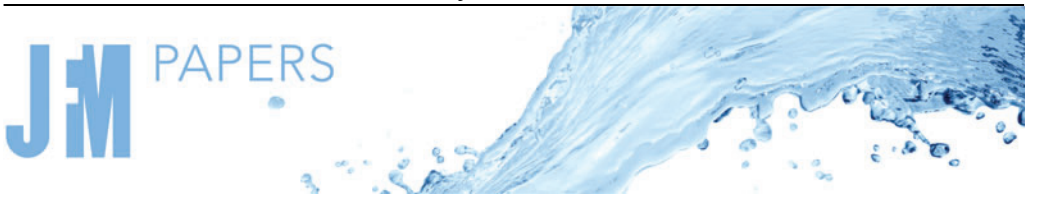

Air-jet impact craters on granular surfaces: a universal scaling

Prasad Sonar[1],† **and Hiroaki Katsuragi**[1],†

[1]Department of Earth and Space Science, Osaka University, 1-1 Machikaneyama, Toyonaka, Osaka 560-0043 Japan

(Received 26 April 2024; revised 30 July 2024; accepted 6 September 2024)

Craters form as the lander's exhaust interacts with the planetary surfaces. Understanding this phenomenon is imperative to ensuring safe landings. We investigate the crater morphology, where a turbulent air jet impinges on granular surfaces. To reveal the fundamental aspect of this phenomenon, systematic experiments are performed with various air-jet velocities, nozzle positions and grain properties. The resultant crater morphology is characterized by an aspect ratio. We find a universal scaling law in which the aspect ratio is scaled by a dimensionless variable consisting of the air velocity at the nozzle, the speed of sound in air, the nozzle diameter, the nozzle-tip distance from the surface, the grain diameter, the density of the grains and the density of air. The obtained scaling reveals the cross-over of the length scales governing the crater aspect ratio, providing a useful guideline for ensuring safe landings. Moreover, we report a novel drop-shaped sub-surface cratering phenomenon.

Key words: granular media, complex fluids

1. Introduction

People aspire to live on the Moon. To achieve this, we need to develop safe landing mechanisms. Ensuring sustainable and safe landings provides infinite opportunities for further space exploration. However, attaining a stable landing on a planetary surface stands as a paramount concern in the realm of space immigration. Interaction between the lander's exhaust and planetary surface is a key component of this problem. The chosen landing site usually consists of a flat and crater-free terrain (Toigo & Richardson 2003). Nonetheless, the plume ejected from a descending spacecraft has the potential to induce cratering and splashing, leading to a potentially unstable landing scenario. It is necessary to conduct a thorough assessment of the cratering and regolith grain splashing induced by

† Email addresses for correspondence: prasadrsonar@gmail.com, katsuragi@ess.sci.osaka-u.ac.jp

an air jet on a planetary surface. To explore the inherent nature of this type of phenomenon, it is essential to uncover a universal scaling framework for the granular cratering caused by the impact of air jets. However, accurately replicating a fully realistic landing scenario is difficult. Consequently, researchers usually perform small-scale laboratory experiments to explore scaling relationships. This study is dedicated to investigating granular cratering resulting from air-jet impact by a small-scale experiment. Through systematic analysis of laboratory-scale experiments, we derive a universal scaling law governing the crater morphology. The obtained scaling includes newly defined scaling parameters and offers a novel direction for research on the interaction between a fluid and granular matter. In addition, this scaling would allow us to anticipate the potential landing scenarios on various planetary surfaces in future space missions.

Crater formation due to an impact is an extremely complex phenomenon (Holsapple & Schmidt 1982; Croft 1985; Uehara *et al.* 2003; Lohse *et al.* 2004; Katsuragi 2016; Prieur *et al.* 2017; Van Der Meer 2017; Yamamoto *et al.* 2017; Allibert *et al.* 2023). Jet impact crater formation further involves the interaction between a continuously impinging pressurized fluid and a granular surface, which results in a bowl-shaped depression. The crater shape varies with the properties of the target material and the impinging fluid. Landing rockets on planetary surfaces and erosion near hydraulic structures are important examples relating to jet-impact-induced cratering (Rajaratnam & Beltaos 1977; Lane *et al.* 2010; Badr, Gauthier & Gondret 2014*a*,*b*; LaMarche & Curtis 2015; Gorman *et al.* 2023; Metzger 2024*a*). Here, we focus on the cratering phenomena that may cause problems during the landing and re-launching of rockets. Particularly, hardware damage to the rocket body or its sensors can be caused by large amounts of dust kicked up by exhaust plumes. Understanding this type of plume–surface interaction (PSI) process is one of the most important issues in the space engineering field (Donohue, Metzger & Immer 2021; Baba *et al.* 2023; Gorman *et al.* 2023; Bajpai, Bhateja & Kumar 2024). Indeed, dust ejecting up onto the sensors was one of the many reasons for recent landing failures on the lunar surface (Witze 2023; Metzger 2024*b*).

The granular crater formation caused by the fluid impact has been studied by many researchers (Rajaratnam & Beltaos 1977; Metzger *et al.* 2009; Lane *et al.* 2010; Metzger, Smith & Lane 2011; Zhao, Zhao & Liu 2013; Badr *et al.* 2014*a*,*b*; Clark & Behringer 2014; LaMarche & Curtis 2015; Badr, Gauthier & Gondret 2016; Guleria & Patil 2020; Donohue *et al.* 2021; Gong *et al.* 2021; Benseghier *et al.* 2023). Various mechanisms reported for crater formation include viscous erosion (VE), diffused gas eruption (DGE), bearing capacity failure (BCF) and diffusion-driven shearing (Metzger *et al.* 2009; Lane *et al.* 2010; Metzger *et al.* 2011; Kuang *et al.* 2013). The VE is the most common and most investigated (Zhao *et al.* 2013; Badr *et al.* 2014*a*,*b*; Clark & Behringer 2014; Badr *et al.* 2016). The cratering process is controlled by the conditions of the impinging jet and erodible granular bed. During crater erosion, both the crater depth and diameter grow with time and approach the asymptotic values (Zhao *et al.* 2013; Badr *et al.* 2014*a*; Donohue *et al.* 2021; Gorman *et al.* 2023). The scaling laws for crater morphology were studied based on the Froude, Shields and erosion numbers (Clark & Behringer 2014; Guleria & Patil 2020; Gong *et al.* 2021). However, these scaling relationships are applicable only to each specific condition. There is a lack of consistency across various experiments, hindering the establishment of a unified understanding among these previous studies. The pursuit of universal scaling relations for granular cratering induced by air-jet impact is a critical issue and intersects both fundamental granular physics and space engineering. In this paper, we propose a unified scaling relation for jet-induced granular cratering, to better understand the PSI process. Particularly, new dimensionless parameters are introduced to

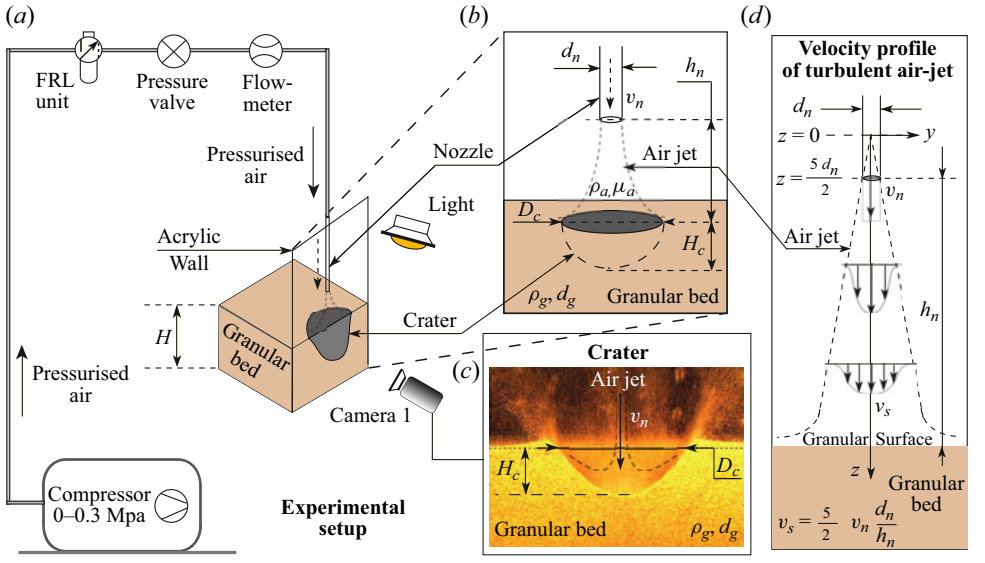

Figure 1. (*a*) The schematic of the experimental set-up for air-jet impact experiments in a three-dimensional half-space set-up, (*b*) a magnified view of the cratering process, (*c*) an example image of a crater and (*d*) a sketch of the impinging air-jet configuration.

aim at providing universal explanations for the systematic experimental results. Besides, we report a novel sub-surface cratering phenomenon as well.

The rest of the paper is organized as follows: in the next section, the experimental set-up, materials and procedures are introduced. In § 3, we define the various kinds of craters formed and discuss a scaling analysis for crater dimensions using well-known non-dimensional numbers. Then, we propose a unified scaling law for the crater's aspect ratio that characterizes the crater morphology. In § 4, we discuss the advantages of the improved scaling relation, further improvements that can be done and a novel drop-shaped crater that we encounter. Finally, we conclude in § 5.

2. Experiments

We systematically perform laboratory-scale experiments to form air-jet-induced craters. Figure 1 shows the schematic of the experimental set-up. We perform experiments in a three-dimensional (3-D) half-space set-up to capture crater images. The rectangular container of inner dimensions $240 \times 200 \times 70\ \mathrm{mm}^3$ contains the granular material, which serves as a planetary surface simulant. The compressed air jet, mimicking the nozzle exhaust, is directed vertically downwards along the acrylic wall, keeping a minimum distance of approximately 1 mm between the nozzle and the acrylic wall while minimizing the influence of the wall on the central jet velocity (Rajaratnam & Beltaos 1977; Schlichting & Gersten 1979; LaMarche & Curtis 2015; Guleria & Patil 2020). The formation of boundary layer along the wall is discussed separately in Appendix A.1. The pressure-controlled air jet of 0.01–0.3 MPa pressure range comes out through a nozzle. We vary the nozzle diameter, d_n, to control the impinging air-jet velocity, v_n. The distance between the granular surface and the nozzle tip, h_n, is also varied. The variation in h_n captures the dynamic advancement of the rocket towards the landing surface. As shown in figure 1(*b*), the air jet is directed onto a granular bed of grain size d_g and true density ρ_g.

Grains	d_g (mm)	ρ_g (g cm^{-3})	Shape	φ_i	θ (deg.)
1. BZ02	0.17–0.25	2.60	Sphere	0.66	21.8 ± 0.7
2. BZ08	0.71–0.99	2.60	Sphere	0.63	21.6 ± 0.7
3. BZ1	0.99–1.39	2.60	Sphere	0.63	19.7 ± 0.3
4. BZ2	1.50–2.50	2.60	Sphere	0.62	19.2 ± 0.2
5. SUS304	$\simeq 1$	7.60	Cylinder	0.74	30.0 ± 0.3
6. Sand	0.16–0.30	2.63	Irregular	0.63	29.0 ± 1.6

Table 1. Properties of granular materials.

Parameters	Operational range
1. Air-jet velocity, v_n	19–375 m s^{-1}
2. Nozzle diameter, d_n	2–6 mm
3. Nozzle height, h_n	10–200 mm
4. Grain diameter, d_g	0.16–2.5 mm
5. Grain density, ρ_g	2.6 and 7.6 g cm^{-3}
6. Grain shape	spherical, cylindrical and irregular

Table 2. Operational range of control parameters.

Upon jet–surface interaction, figure 1(*c*) captures the formation of the crater of width D_c and depth H_c from the initial surface level (dotted line). In this study, we focus on the steady crater shapes, i.e. constant D_c and H_c conditions. The steady crater shape is immediately developed within a few seconds. Due to its greater tendency to erode, finer and lighter granular material needs more time to reach a steady state than the coarser and heavier grains.

Table 1 shows the properties of the grains used in the experiments. The initial packing fraction and angle of repose are denoted by φ_i and θ, respectively. The BZ series and SUS304 represent spherical glass beads and cylindrical steel-cut-wire beads, respectively, whereas the sand is the irregular-shaped Toyoura sand. The initial volume fraction, as mentioned in table 1, would remain approximately the same as the uncertainty of the mass in the container is observed to be less than 1 % during random sampling measurements.

The experiments are conducted in the following sequence. We first fill the container by pouring the grains and precisely maintaining the flat surface. The nozzle tip of d_n is placed at h_n. Then, the cratering induced by the air-jet impact is recorded by the camera (STC-MCCM401U3V) that captures side-view images at 200 fps with a spatial resolution of 0.058 mm pixel^{-1} and 2048×2048 image size. As shown in figure 1(*c*), D_c is the width of the crater cavity at the initial horizontal surface level (dotted line) and H_c is the depth of the cavity measured vertically down from the initial surface level. During every experiment, an air jet impinges the granular bed for 10 s. See tables 3 and 4 in Appendix A.2 for more details of the experimental conditions. We consider the average of five measurements taken for each experimental condition. A total of more than 700 experiments are carried out. Table 2 shows the range of control parameters in the experiments. Further details regarding experiments can be found in Appendix A.2.

3. Results

Figure 2(*a*) shows a phase diagram of various crater types for varying h_n and M_n, where $M_n = v_n/C$ is the dimensionless air-jet velocity at the nozzle and $C = 343$ m s^{-1} is the

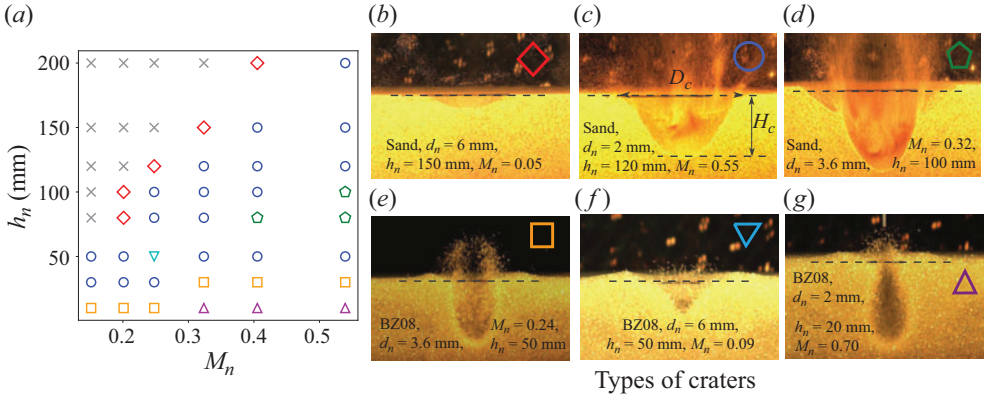

Figure 2. (*a*) Phase diagram shows craters formed when a pressurized air jet is directed through the nozzle ($d_n = 3.6$ mm) onto SUS304 grains. Various shapes of craters observed over a range of experimental conditions are: (*b*) saucer, (*c*) parabola, (*d*) parabola with the intermediate region, (*e*) U-, (*f*) V- and (*g*) drop-shaped craters. The ×, grey symbols correspond to no-crater formation. In the phase diagram, h_n represents the distance from the nozzle tip to the granular surface, and $M_n = v_n/C$ is the dimensionless air-jet velocity at the nozzle, where $C = 343$ m s^{-1} is the speed of sound in air.

speed of sound in air. As shown in figure 2(*b–g*), we observe six types of craters. Five of these, figure 2(*b–f*), are already documented in the literature (Lane *et al.* 2010; Clark & Behringer 2014; Guleria & Patil 2020). We reproduce these results over a broader range of parameters, i.e. by exploring all the controlling variables mentioned in table 2 that span a considerably wide range of at least over a decade. As seen in figure 2(*a*), the 'parabola' craters (○, blue) and the parabola with 'intermediate' region craters (⬠, green) are observed most frequently within the current parametric range. However, 'V-shaped' craters (▽, cyan) are formed more frequently for finer grains (see figures 10 and 11 in Appendix B for all phase diagrams and the congregated phase diagram, respectively). The 'saucer'-type wide and shallow craters (◇, red) and 'U-shaped' narrow and deep craters (□, orange) are formed at high and low h_n ranges, respectively. Moreover, we find a novel crater shape (figure 2*g*), the 'drop-shaped' cavity, beneath the granular surface (△, magenta), which has not been reported in the literature yet. While we also observe 'truncated-shape' craters due to the size limit of the experimental set-up (see figure 12*a*,*b* in Appendix C), we exclude these truncated craters from the following analysis because the crater's depth H_c cannot be measured for them. The details and movies related to various types of crater formation can be found in Appendix D and the supplementary material (SM) available at https://doi.org/10.1017/jfm.2024.906.

Now, considering the varied and complex range of craters, we analyse the crater morphology and its governing parameters in detail. To obtain the scaling relation, we introduce two dimensionless numbers, $G_n = d_n/h_n$ and $r = \rho_g/\rho_a$, where $\rho_a = 1.2$ kg m^{-3} is the air density. The parameter G_n relates to the velocity profile of the turbulent jet, as shown in figure 1(*d*). The velocity of the air jet would reduce to $v_s = (5/2)M_n\, G_n\, C$ (for turbulent jets, the universal angle of a diverging cone is approximately 24 °. Thus, the initial jet radius and the downstream distance z from the nozzle exit are related by a constant $\tan(12°) \sim 1/5$. The distance z is counted not from the nozzle exit but from a distance $5d_n/2$ into the nozzle. This point of origin is called the virtual source (Cushman-Roisin 2014). We use this axisymmetric model for our 3-D half-space experimental set-up as a first step to investigate the scaling relation) at the surface of the

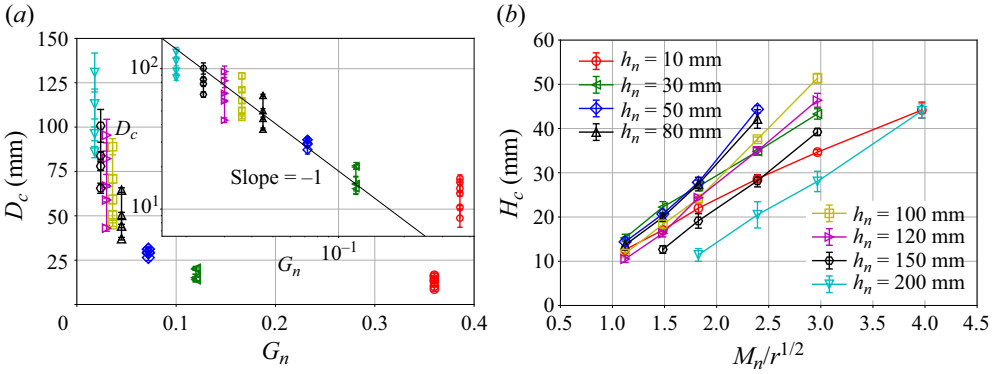

Figure 3. The scaling relations among D_c, H_c, $G_n = d_n/h_n$, M_n and $r = \rho_g/\rho_a$ are presented. Panels (*a*,*b*) suggest the scaling relations as $D_c \sim G_n^{-1}$ and $H_c \sim (M_n/r^{1/2})^1$, respectively. The inset of (*a*) shows a plot of the same data on a log–log scale. The data shown in (*a*,*b*) originate from the experiments performed with BZ1 grains using $d_n = 3.6$ mm.

granular bed (Cushman-Roisin 2014). By using r, a dimensionless number proportional to the dynamic pressure of the air jet, $\rho_a v_n^2$, can be expressed by $(M_n/r^{1/2})^2$. From the measured data, we find that D_c and H_c can be scaled as $D_c \sim G_n^{-1}$ and $H_c \sim M_n/r^{1/2}$. Figures 3(*a*) and 3(*b*) shows the relations D_c vs G_n and H_c vs $M_n/r^{1/2}$, respectively. Namely, D_c is mainly governed by the air-jet geometry and H_c is principally determined by the dynamic pressure of the impinging air jet. From these relations, we investigate a scaling law for the crater's aspect ratio $R_c = D_c/H_c$. For the safe rocket landing situation, large-R_c (shallow and flat) cratering causes the ejecta to flow radially outward and is thus preferred over vertically ejected grains that might cause the malfunction of the lander as in the case of deep crater formation. Therefore, R_c is the most important parameter characterizing this type of cratering.

The roles of conventional dimensionless numbers have been thoroughly investigated by researchers (Badr *et al.* 2016; Guleria & Patil 2020; Gong *et al.* 2021). They used the Froude number $Fr = v_n/\sqrt{gd_g}$, the Shields number $Sh = Fr\sqrt{\rho_a/(\rho_g - \rho_a)}$ and the Reynolds number $Re = \rho_a v_n d_n/\mu_a$, where g is the gravitational acceleration and μ_a is the viscosity of air. For our case, we observe that the Re, Fr and Sh are not sufficient to scale R_c since h_n is not included in these dimensionless numbers; as shown in figures 4(*a*)–4(*c*), respectively. In addition, while studying the temporal evolution of a crater formed by rocket exhaust, Rajaratnam *et al.* introduced an erosion number $E_c = Sh\, G_n$, which incorporates various relevant parameters (Rajaratnam & Beltaos 1977; Donohue *et al.* 2021). However, during an experimental investigation of the growth rate of the crater, Donohue *et al.* indicated that E_c may not accurately characterize the crater formation (Donohue *et al.* 2021). Remarkably, focusing on the crater morphology observed in this paper, the erosion number, E_c, indeed shows promising results but only when one kind of granular surface is considered (see figure 4*d*). Yet, figure 5 suggests that the data scatter for other experimental parameters.

Now, we consider a more appropriate choice for a scaling law. From figures 3(*a*) and 3(*b*), $D_c \sim G_n^{-1}$ and $H_c \sim M_n/r^{1/2}$ results in the combined scaling $R_c \sim (M_n\, G_n/r^{1/2})^{-1}$. Figure 6 shows the scaling $R_c \sim (M_n\, G_n/r^{1/2})^{-1}$. One can confirm the reasonable data collapse, particularly in the small $M_n\, G_n/r^{1/2}$ regime. The obtained scaling is almost consistent with the numerical simulation of air-jet impact onto a granular bed (Kuang *et al.* 2013); see the filled ⬠, black in figure 6. Although this scaling reasonably collapses the

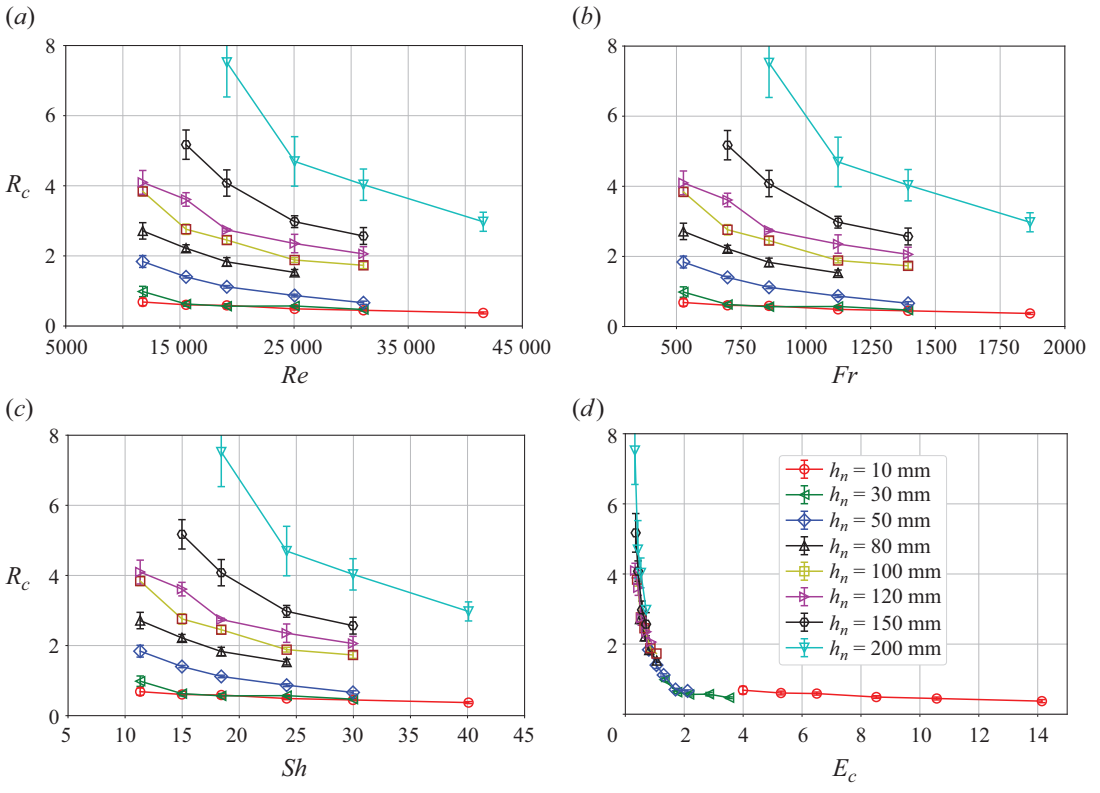

Figure 4. Crater's aspect ratio, R_c, vs (*a*) Re, (*b*) Fr, (*c*) Sh and (*d*) E_c. Experiments are performed for BZ1 and $d_n = 3.6$ mm.

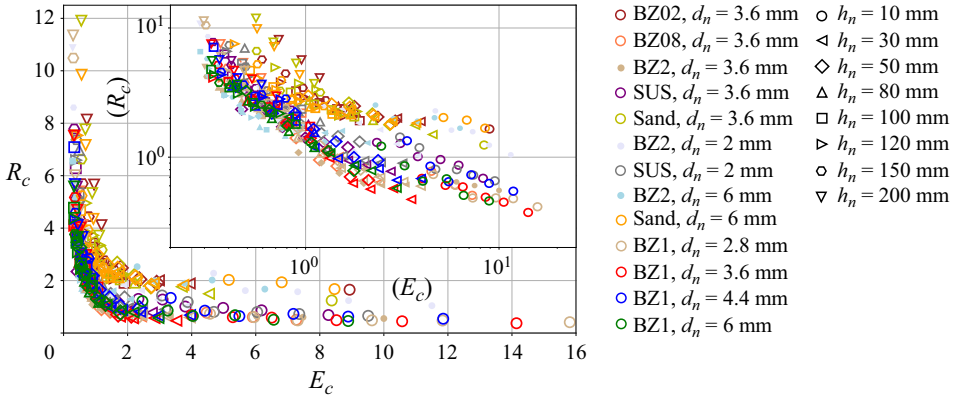

Figure 5. The aspect ratio, R_c, is plotted as a function of E_c. A certain degree of collapse can be observed, but the quality of the data collapse is not very good. Inset shows a plot of the same data on a log–log scale. The shape of symbols represents various h_n values.

experimental data, we realize the data for small h_n (filled circular symbols) systematically deviate from the scaling.

To obtain a better scaling, R_c at the smallest $h_n (= 10$ mm) is further analysed. We find the average of R_c at $h_n = 10$ mm, $\bar{R}_c^{h10}$ is scaled as $\bar{R}_c^{h10} \sim (r\delta)^{1/2}$, where $\delta = d_n/d_g$.

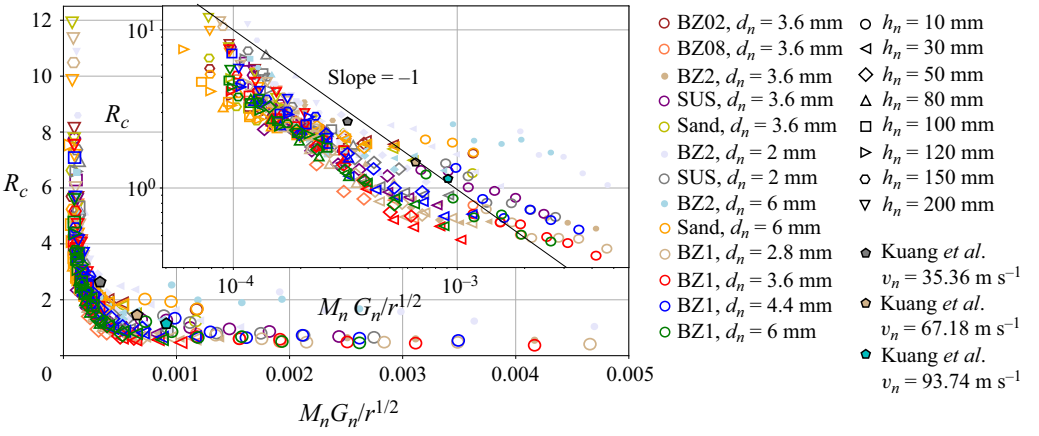

Figure 6. The crater aspect ratio R_c of all experiments is plotted as a function of $M_n\,G_n/r^{1/2}$. Inset shows a plot of the same data on a log–log scale. The colour indicates the target material and d_n conditions. The shapes of the symbols represent h_n values. The filled circular symbols represent data for $h_n = 10$ mm for each corresponding colour condition.

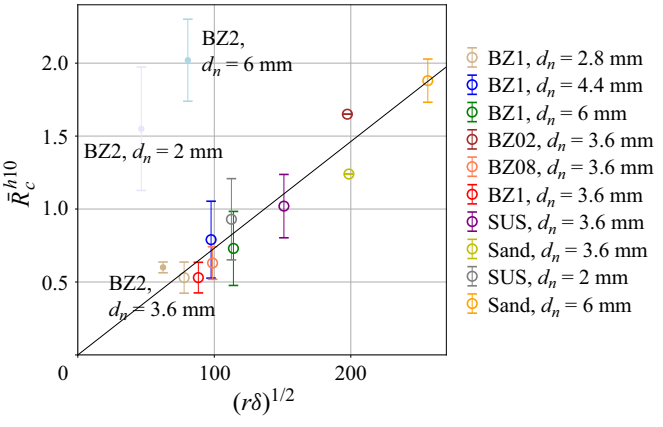

Figure 7. The average of aspect ratio R_c at $h_n = 10$ mm; $\bar{R}_c^{h10}$, is plotted as a function of $(r\delta)^{1/2}$.

Figure 7 clearly indicates the scaling $\bar{R}_c^{h10} \sim (r\delta)^{1/2}$ except for the largest grains BZ2 ($d_g = 2$ mm). This scaling in the small h_n regime results from switching of the relevant length scale from h_n to d_g, as h_n decreases. Thus, as the lander approaches the surface, the grain size becomes more significant compared with the nozzle height.

The form of scaling $R_c = (r\delta)^{1/2} = (\rho_g d_n/(\rho_a d_g))^{1/2}$ is slightly puzzling. The density and length scale of the air jet and grains are not naturally linked to the crater's aspect ratio. This counter-intuitive correlation could originate from the deformability of the impactor (Katsuragi 2010), as well as the mixing of the granular substrate and the impactor (Nefzaoui & Skurtys 2012; Zhao *et al.* 2015*a*; Zhao, de Jong & van der Meer 2015*b*, 2017; Van Der Meer 2017). For example, cratering by a droplet impact on a permeable substrate also shows a similar inverse tendency (Katsuragi 2010). Specifically, a similar density dependence of the crater radius formed by droplet impact was reported. Namely, the larger crater diameter was observed for larger ρ_g. Recently, Zhao *et al.* performed experiments to study droplet impact on sand (Zhao *et al.* 2015*b*, 2017). It was observed that liquid–grain

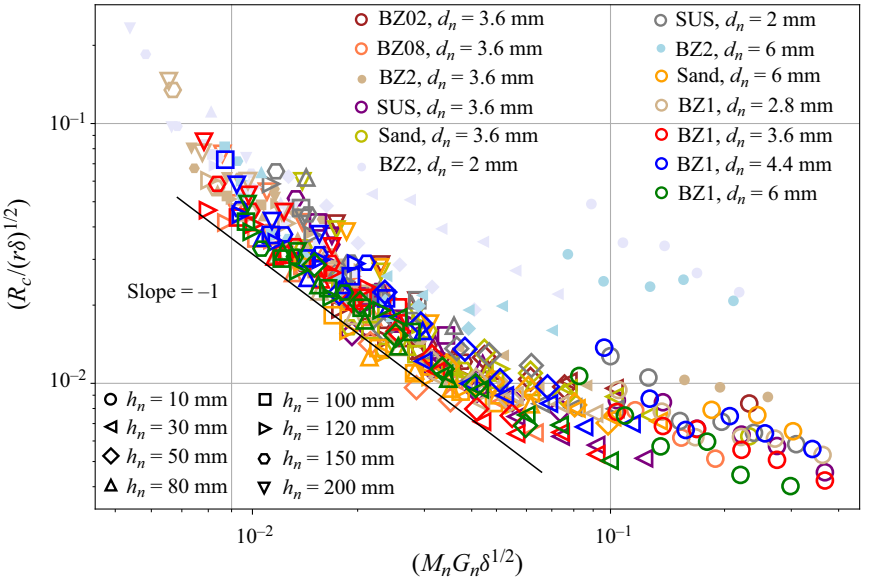

Figure 8. The scaling relation of (3.1), $R_c/(r\delta)^{1/2} = f(M_nG_n\delta^{1/2})$, is presented for all experimental data. Except for the largest grain data (BZ2, $d_g = 2$ mm, filled symbols in the plot), all the data obey the scaling. The shape of the symbols represents various h_n values.

mixing suppresses droplet spreading and splashing. During the experiments, the packing density of the granular target, grain size, wettability conditions and the impact velocity are varied. It was found that, by increasing the grain size and the wettability conditions, the maximum droplet spreading undergoes a transition from a capillary regime towards a viscous regime. This complex interaction between droplet intruder and granular target creates various crater morphologies (Zhao *et al.* 2017). These tendencies could be typical difficulties in soft-impact studies. In our case, high-velocity air can penetrate the shallow layers of the permeable granular substrate with more ease than can a water droplet. The low dynamic viscosity of air, compared with water or other liquids, allows for easier permeation of the granular bed, viewed as a porous medium. This prolonged presence of jet air within the subsurface layers while the crater is being formed may alter the local properties of the granular target during crater formation. Thus, the empirical scaling obtained here can be used to formalize the scaling better than the previously proposed ones.

Finally, we derive the unified scaling law based on the above-mentioned scaling results. The combined scaling function is written as

$$\frac{R_c}{(r\delta)^{1/2}} = f\left(M_nG_n\delta^{1/2}\right), \tag{3.1}$$

where the function $f(x)$ satisfies $f(x) \sim x^{-1}$ in the small x regime and $f(x) \simeq$ const. in the large x regime. This functional form indeed recovers $R_c \sim (M_nG_n/r^{1/2})^{-1}$ at large h_n and $R_c \sim (r\delta)^{1/2}$ at small h_n. In figure 8, the scaling cross-over point is $M_nG_n\delta^{1/2} \simeq 10^{-1}$. Therefore, the cross-over h_n can be computed as $h_c \simeq 10M_n\delta^{1/2}d_n$. In such a complex PSI process, capturing a shift in the relevant length scale and its cross-over point is an important takeaway of this paper.

When the grain size is the largest (BZ2 grains), however, the data cannot be scaled (filled symbols in figure 8). This indicates that the cratering dynamics is completely different

when $d_g \sim d_n$. Namely, d_n must be sufficiently greater than d_g to safely apply the obtained scaling. This result is informative to provide the lower limit of the nozzle size in the lander design.

4. Discussion

The unified scaling law presented in figure 8 (and (3.1)) is superior to the previously reported scaling laws that are based on conventional dimensionless numbers.

Moreover, from the fluid mechanics perspective, these scaling relations can be further investigated to study the grain motion and convection currents during the temporal evolution of the different types of craters. In addition, our result shows the cross-over of scaling laws, which may be of interest to researchers studying soft matter physics (Maruoka 2023). By using the obtained scaling, $R_c \sim (M_n G_n / r^{1/2})^{-1}$, we can estimate R_c mainly from the jet conditions in the large h_n regime. We do not need detailed information about the landing surface. Having a simple scaling parameter mainly consisting of jet conditions is advantageous to reducing uncertainty in space missions. Within the approachable distance, we should use the relation $R_c \sim (r\delta)^{1/2}$, i.e. grain size information is necessary in the small h_n regime.

The 3-D half-space experimental set-up has limitations, such as the presence of an acrylic wall that forms a boundary layer affecting the jet's velocity structure. Thus, this set-up might break the axisymmetric assumption for the jet. This may affect the surface erosion and the crater dimensions. We believe that by addressing such experimental limitations, the current scaling relations (in figure 8) may further be improved by reducing data scatter around the scaling. To consider a realistic rocket landing application, we have to estimate the ejection speed, angle, etc. Besides, the effects of gravity and ambient air must be evaluated. In this experiment, dimensionless numbers including the gravity effect (Fr, Sh, and E_c) do not work well to collapse the data (figures 4 and 5). As demonstrated in Baba *et al.* (2023), however, air-jet cratering and the resultant ejection process are significantly affected by the gravity condition. Modification of the obtained scaling and the precise measurement of ejector behaviour are the important next steps to consider in an actual landing application. The scaling function developed in this study provides a starting point for further investigations.

As mentioned earlier, we observe a novel drop-shaped sub-surface cratering phenomenon on a few occasions, especially when the nozzle tip is very close to a granular surface (see $\blacktriangle$, magenta in figure 2*a*) consisting of coarser/denser grains. In low h_n cases, the turbulent jet impinges on the granular surface at high v_s. In the case of coarser grains, the larger pores between the grains allow easier penetration of the high-velocity turbulent air jet. Then, the jet penetrates through the surface and expands beneath. In contrast, a granular surface made of finer grains is easy to erode. In such a case, the air escapes out while eroding the surface and a drop-shaped cavity cannot be formed. The denser and coarser SUS304 grains are difficult to displace, but allow the trapped air to deform the sub-surface material (see figure 12*c* in Appendix C).

The drop-shaped crater can be attributed to the BCF or DGE mechanisms (Alexander, Roberds & Scott 1966; Scott & Ko 1968; Metzger *et al.* 2009). However, BCF forms craters with long and narrow cylindrical shapes when a pressurized rocket exhaust pushes the soil down into a depression. In contrast, we observed convection currents within the drop-shaped craters with narrow D_c and minor displacement of the grains around the drop cavity as air diffuses into the material. Thus, we believe this phenomenon can be related to the DGE (Scott & Ko 1968; Metzger *et al.* 2009), which usually causes an

annular-ring eruption around the jet. However, we have not seen such eruptions in our small-scale experiments. Further study is necessary to reveal the physical mechanism governing the drop-shaped crater. In addition, this intriguing phenomenon is particularly significant to understanding the rocket launch scenarios from planetary surfaces, where sudden high-speed exhaust thrust needs to be applied on the unknown granular surfaces from a closer range. Moreover, this phenomenon may be of particular importance on small bodies such as asteroids, which have mostly porous structures.

5. Conclusion

We conclude that the crater morphology produced by an air-jet impact on a granular surface is primarily governed by the combination of the dimensionless air-jet velocity, $M_n = v_n/C$, nozzle geometric factor, $G_n = d_n/h_n$, density ratio between the granular target and air jet, $r = \rho_g/\rho_a$, and the diameter ratio between the nozzle and grain, $\delta = d_n/d_g$. We obtain the scaling $R_c \sim (M_n G_n/r^{1/2})^{-1}$, which is useful to estimate the excavation condition by simple scaling parameters, as long as the nozzle tip is away from the granular surface. Moreover, we find that, within the approachable distance of the granular surface, R_c is governed by $(r\delta)^{1/2}$. This means that the relevant length scale governing crater morphology switches from h_n to d_g on approaching the granular surface. Finally, a unified scaling function involving both scaling relations is established (3.1). The obtained scaling is applicable when $d_n > d_g$. In addition, we find a novel drop-shaped cratering phenomenon that has potential significance in jet impact physics.

Supplementary movies. Supplementary movies are available at https://doi.org/10.1017/jfm.2024.906.

Funding. This work was supported by the JSPS KAKENHI, grant nos. JP18H03679 and JP24H00196 and JSPS-DST Bilateral Program, grant no. JPSJBP120227710.

Declaration of interests. The authors report no conflict of interest.

Author ORCIDs.
Prasad Sonar https://orcid.org/0000-0001-6276-6755;
Hiroaki Katsuragi https://orcid.org/0000-0002-4949-9389.

Appendix A. Experimental conditions

A.1. *Boundary layer*

We use a 3-D half-space experimental set-up that allows us to capture the evolution of the crater and measure the crater's diameter, D_c, and depth, H_c. However, unlike in the case of the free jet in the complete 3-D space, when the turbulent air jet flows parallel to the acrylic wall with one edge of a nozzle close to the wall, it forms a wall jet (Rajaratnam & Beltaos 1977; Schlichting & Gersten 1979; Launder & Rodi 1983; Yue 2001; Barenblatt, Chorin & Prostokishin 2005; Guleria & Patil 2020). A pressure difference causes the jet to deflect towards a boundary that establishes a wall jet at some distance from the nozzle outlet. A wall jet is usually a combination of two distinct layers: an inner boundary layer along the wall and an outer free jet flow layer. These two layers are separated by a mixing layer, where the velocity is close to the maximum (Barenblatt *et al.* 2005). We are interested in a fully developed jet that would hit the granular surface with the maximum velocity. The wall jet itself is a very complex phenomenon that is being studied to understand its implications (Launder & Rodi 1979; Schlichting & Gersten 1979; Launder & Rodi 1983; Barenblatt *et al.* 2005). Boundary layer formation along the wall is one such effect. For turbulent flows along the wall, the boundary layer thickness (Schlichting & Gersten

No.	P_s (MPa)	P (MPa)	Q (lpm)	v_n (m s^{-1})	$M_n = v_n/C$	$Re = \rho_a v_n d_n/\mu_a$
1	0.30	0.25	110.5 ± 1.2	184.7 ± 2.0	0.53	41 573
2	0.20	0.18	82.6 ± 0.6	138.1 ± 1.1	0.40	31 077
3	0.15	0.13	66.6 ± 0.4	111.3 ± 0.7	0.32	25 048
4	0.10	0.09	50.8 ± 0.4	84.9 ± 0.6	0.24	19 108
5	0.07	0.06	41.3 ± 0.2	69.0 ± 0.3	0.20	15 536
6	0.04	0.03	31.2 ± 0.2	52.1 ± 0.3	0.15	11 741

Table 3. Air-jet parameters at $d_n = 3.6$ mm.

No.	P_s (MPa)	P (MPa)	Q (lpm)	v_n (m s^{-1})	$M_n = v_n/C$	$Re = \rho_a v_n d_n/\mu_a$
1	0.30	0.26	115.8 ± 2.9	69.6 ± 1.7	0.20	26 123
2	0.20	0.18	85.4 ± 1.1	51.4 ± 0.7	0.14	19 284
3	0.15	0.13	69.7 ± 0.8	41.9 ± 0.5	0.12	15 742
4	0.10	0.09	52.4 ± 0.4	31.6 ± 0.2	0.09	11 865
5	0.07	0.06	42.3 ± 0.3	25.4 ± 0.2	0.07	9951
6	0.04	0.03	32.0 ± 0.07	19.2 ± 0.04	0.05	7236

Table 4. Air-jet parameters at $d_n = 6$ mm.

1979) is given by $\delta_y = 0.37\ (h_n/{Re_y}^{1/5})$, where $Re_y = v_n h_n/\nu$ is the Reynolds number and ν is the kinematic viscosity of air. For the 3-D half-space experiments, where the jet is close to the wall, considering the maximum jet length as ours, i.e. $h_n = 200$ mm, the boundary layer thickness ranges from 1.1 to 2.3 mm for the highest and lowest jet velocities, respectively. The maximum value of δ_y goes down to 1.3 mm for $h_n = 100$ mm at the same lowest velocity. The reduced velocity at the boundary layer may affect the erosion of the granular surface and, thus, the crater dimensions. Therefore, a minimum distance is kept between the nozzle and the acrylic wall to ensure that a wall jet is not established immediately at the nozzle exit but at some distance ahead that would help reduce the significant effects on crater formations. This way, we can reduce the unwanted influence of the wall and the inner layer on the core region of the jet as much as possible, especially for large h_n cases.

A.2. *Parametric conditions*

As shown in figure 1(*a*) of the main text, the air is compressed and cleaned by the compressor (HG-DC991AL) and regulator (FRL unit), respectively. Then, the clean compressed air enters the solenoid valve (CKD, EXA-C6-02C-3), which controls the air pressure. Next, the flow meter (HoribaStec, MF-FP 10NH06-500-AI-ANV3M) measures the flow rate, Q, up to 50 lpm. Using a linear relationship between Q and pressure, P, we extrapolate for Q beyond its original observation range at higher P.

Tables 3 and 4 show six different conditions used to perform the experiments when $d_n = 3.6$ mm and 6 mm, respectively. Due to the limited compressor capacity (36 l), it is difficult to maintain constant pressure while a crater is being formed. All experiments are started at pressure P_s and last for 10 s. As shown in figure 9, the steady crater shape is immediately developed within a few seconds. As shown, various craters reach steady states at different times based on the parametric conditions. Considering the nozzle diameter from 6 to 2 mm, the total time required to drop the pressure from 0.3 to

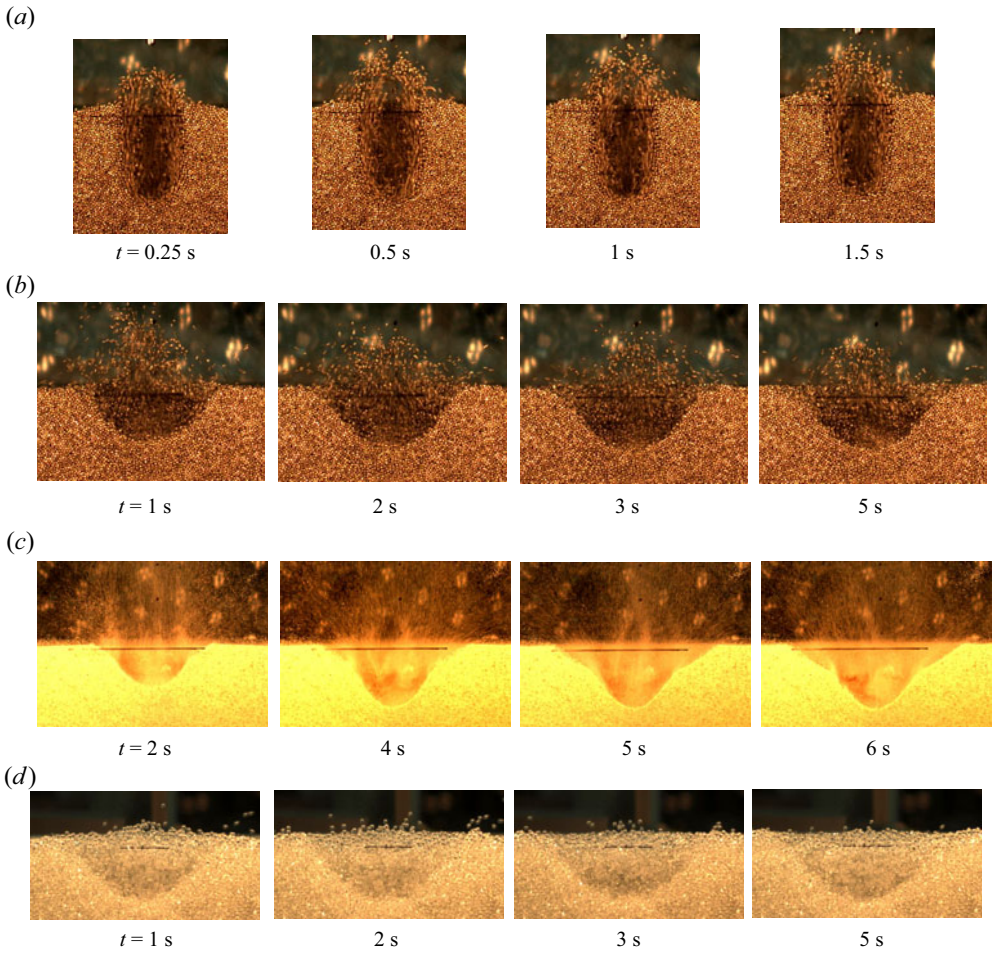

Figure 9. The timeline for various craters to achieve a steady state. (*a*) U-shaped crater, SUS304, $d_n = 3.6$ mm, $h_n = 30$ mm, $M_n = 0.53$. (*b*) Parabolic crater, SUS304, $d_n = 3.6$ mm, $h_n = 100$ mm, $M_n = 0.40$. (*c*) Intermediate crater, sand, $d_n = 6$ mm, $h_n = 100$ mm, $M_n = 0.12$. (*d*) Parabolic crater, BZ2, $d_n = 2$ mm, $h_n = 120$ mm, $M_n = 0.70$.

0.01 MPa varies from 90 to 120 s, respectively. The pressure range is determined by the controllable range of the solenoid valve and the flow meter. Thus, within this available time range, we perform experiments over six different air-pressure conditions. During this time, the average quantities of pressure P, mass flow rate Q, and v_n are evaluated, with the corresponding dimensionless air-jet velocity at the nozzle (Mach number), $M_n = v_n/C$ and Reynolds number, $Re = \rho_a v_n d_n/\mu_a$, where C is the speed of sound in air, d_n is the nozzle diameter and ρ_a and μ_a are the density and viscosity of air, respectively. We use the speed of sound in air, $C = 343$ m s^{-1}, to non-dimensionalize the air-jet velocity, v_n.

Appendix B. Phase diagrams

Figure 10(*a–l*) shows the phase diagrams of experiments performed with various combinations of granular materials and nozzle parameters d_n and h_n. In general, the 'saucer-shaped' wide and shallow craters (◇, red) and 'U'-shaped narrow and deep craters (□, orange) are formed at higher and lower values of h_n, respectively.

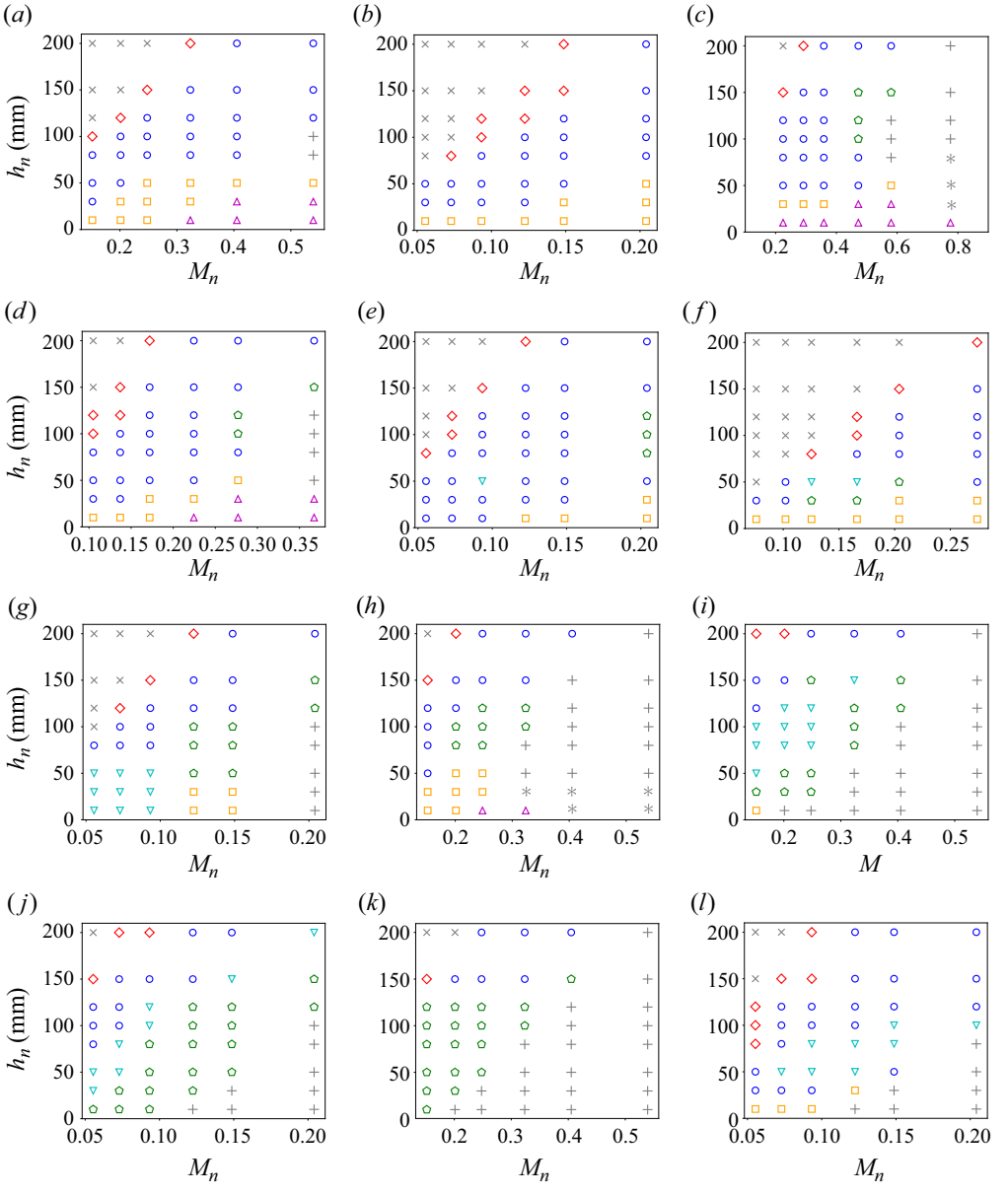

Figure 10. Phase diagrams for the experiments performed over a range of material and controlling parameters. Various shapes of craters observed are: saucer (◇, red), parabola (○, blue), parabola with intermediate region (⬠, green), U-shaped (□, orange), V-shaped (▽, cyan) and drop-shaped crater (△, magenta). The +, grey, ∗, grey and ×, grey symbols correspond to the truncated parabolic craters, truncated drop-shaped craters and no-crater formations, respectively. Example images of parabolic and drop-shaped truncated craters can be found in figure 12(*a*,*b*). Panels show (*a*) BZ2, $d_n = 3.6$ mm; (*b*) BZ2, $d_n = 6$ mm; (*c*) BZ1, $d_n = 2.8$ mm; (*d*) BZ1, $d_n = 4.4$ mm; (*e*) BZ1, $d_n = 6$ mm; (*f*) SUS304, $d_n = 5.2$ mm; (*g*) BZ08, $d_n = 6$ mm; (*h*) BZ08, $d_n = 3.6$ mm; (*i*) sand, $d_n = 3.6$ mm; (*j*) sand, $d_n = 6$ mm; (*k*) BZ02, $d_n = 3.6$ mm; (*l*) BZ02, $d_n = 6$ mm.

The 'parabola-shaped' crater (○, blue) and the parabola with an 'intermediate' region crater (⬠, green) are observed most frequently within the parametric range. However, 'V-shaped' craters (▽, cyan) are formed more frequently for finer grains. For finer grains, truncated craters (+) and truncated drop-shaped craters (∗, grey) are observed at

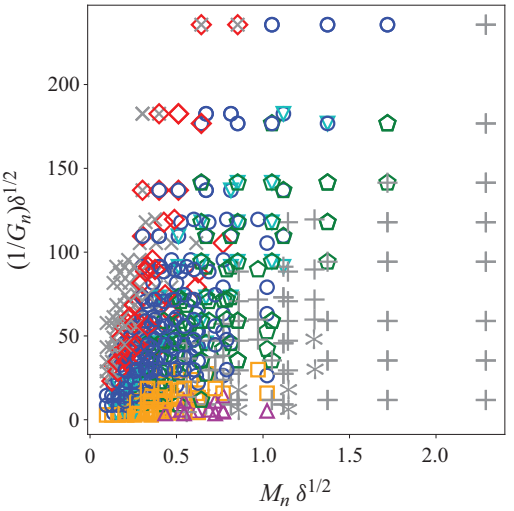

Figure 11. Congregated phase diagram. Various shapes of craters observed are: saucer (◇, red), parabola (∘, blue), parabola with intermediate region (⬠, green), U-shaped (□, orange), V-shaped (filled ∇, cyan) and drop-shaped crater (Δ, magenta). The +, grey, ∗, grey and ×, grey symbols correspond to the truncated parabolic craters, truncated drop-shaped craters and no-crater formations, respectively. In the congregated phase diagram, $\delta = d_n/d_g$, where d_n and d_g are the nozzle and grain diameters, respectively.

high velocities, which corresponds to the large M_n regime. For large h_n and small M_n, the air jet is not able to erode the granular surface to form a crater (represented by ×).

Figure 11 shows congregated data incorporating all phase diagrams presented earlier in the parametric space of $(1/G_n)\,\delta^{1/2}$ and $M_n\,\delta^{1/2}$. While one can confirm the clustering tendencies of the same symbols, it is difficult to define clear borders among crater shapes. However, this information may assist in preplanning the lander's descent based on the possibility of forming a minimal-risk crater shape. This involves controlling the exhaust velocity at the nozzle at different heights above the surface. This would also allow the lander to estimate the time and amount of dust splashing, which may lead to potential malfunction.

Appendix C. Crater images

Figure 12 shows additional experimental images of crater shapes. Figure 12(*a*) shows a truncated drop-shaped crater (∗), where the air jet is strong enough to go through the granular bed and interact with the base of the container. Here, the nozzle position is close to the surface. Thus, the high-velocity turbulent air jet passes through and expands beneath the surface. We call it a truncated drop-shaped crater, as the crater would have assumed a drop shape for a thicker bed thickness. However, if the nozzle is positioned farther from the surface, it causes high erosion at the surface. Thus, the air jet forms the shape of a truncated crater (+) as shown in figure 12(*b*). We do not investigate the truncated crater phenomenon here because the system size clearly affects the result and it is impossible to measure H_c. The data used in this article are only for the complete i.e. non-truncated, craters, where the granular material below the crater shows negligible displacement, and thus, such craters are not affected by the container's base. We experimentally confirm that the crater shape is almost independent of the thickness of the target granular layer in the

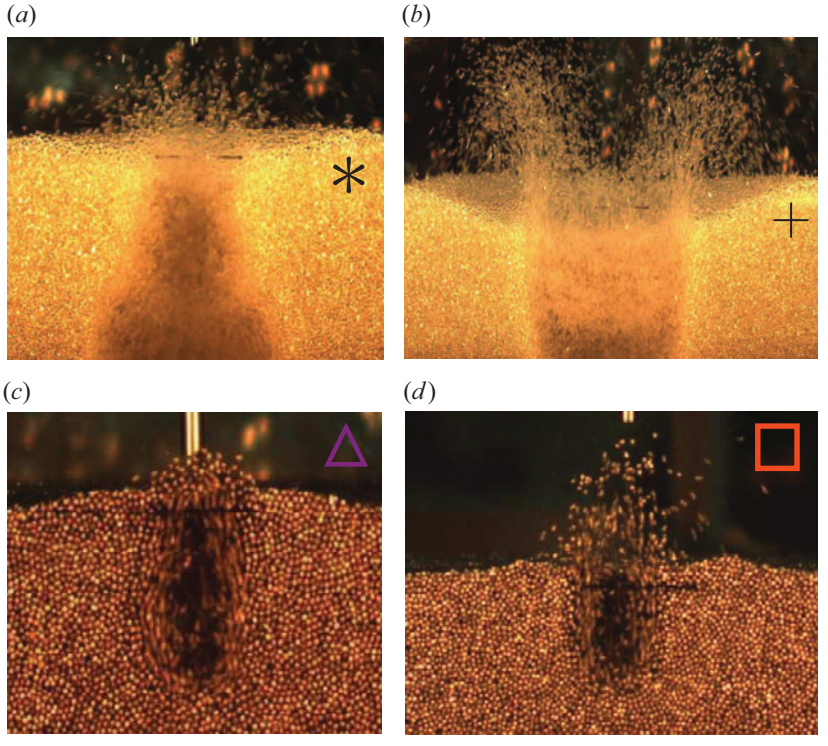

Figure 12. (*a*) Truncated drop-shaped crater (BZ1, $d_n = 2.8$ mm, $h_n = 30$ mm, and $M_n = 0.77$), (*b*) truncated crater (BZ1, $d_n = 2.8$ mm, $h_n = 100$ mm, and, $M_n = 0.77$), (*c*) drop-shaped crater (SUS304, $d_n = 3.6$ mm, $h_n = 10$ mm, and, $M_n = 0.53$) and (*d*) 'U' shaped crater (SUS304, $d_n = 2$ mm, $h_n = 30$ mm, and, $M_n = 0.7$).

Name	Reference	Crater type	Material	d_n (mm)	h_n (mm)	M_n
Movie 1	figure 1(*c*)	Parabola (∘, blue)	Sand	3.6	150	0.40
Movie 2	figure 2(*b*)	Saucer (◇, red)	Sand	6.0	150	0.05
Movie 3	figure 2(*c*)	Parabola (∘, blue)	Sand	6.0	120	0.07
Movie 4	figure 2(*d*)	Intermediate (⌓, green)	Sand	3.6	100	0.32
Movie 5	figure 2(*e*)	U (□, orange)	BZ08	3.6	50	0.25
Movie 6	figure 2(*f*)	V (∇, cyan)	BZ08	6.0	50	0.07
Movie 7	figure 2(*g*)	Drop (Δ, magenta)	BZ08	2.0	20	0.55
Movie 8	figure 12(*a*)	Truncated drop (∗, grey)	BZ1	2.8	30	0.77
Movie 9	figure 12(*b*)	Truncated (+, grey)	BZ1	2.8	100	0.77
Movie 10	figure 12(*c*)	Drop (Δ, magenta)	SUS	3.6	10	0.53
Movie 11	figure 12(*d*)	U (□, orange)	SUS	2.0	30	0.70

Table 5. List of movies corresponding to the crater images discussed in the main text and in the appendices.

50 – 80 mm depth range. Figures 12(*c*) and 12(*d*) show 'drop-shaped' and 'U' shaped craters, respectively, formed with SUS304 material, which has a mass density almost three times greater than that of BZ1 grains.

Appendix D. Crater movies

As listed in table 5, we append short movies corresponding to the images of the crater formations included in the manuscript (figures 1*c* and 2*b–g*) and Appendix C (figure 12*a*,*d*) in the SM. Table 5 includes the movie names individually describing the type of crater formed under specified experimental conditions.

References

Alexander, J.D., Roberds, W.M. & Scott, R.F. 1966 Soil erosion by landing rockets final report. *Tech. Rep.* Hayes International Corporation.

Allibert, L., Landeau, M., R"ohlen, R., Maller, A., Nakajima, M. & Wünnemann, K. 2023 Planetary impacts: scaling of crater depth from subsonic to supersonic conditions. *J. Geophys. Res.* **128** (8), e2023JE007823.

Baba, M., Okita, S., Watanabe, K., Maru, Y., Sawai, S., Mori, O. & Fujita, K. 2023 Microgravity experiment using drop tower and cfd-dem coupled simulation about plume-surface interaction. In *AIAA SCITECH 2023 Forum*. AIAA.

Badr, S., Gauthier, G. & Gondret, P. 2014*a* Erosion of granular bed by a normal jet. In *APS Division of Fluid Dynamics Meeting Abstracts*, pp. R17–002.

Badr, S., Gauthier, G. & Gondret, P. 2014*b* Erosion threshold of a liquid immersed granular bed by an impinging plane liquid jet. *Phys. Fluids* **26** (2), 023302.

Badr, S., Gauthier, G. & Gondret, P. 2016 Crater jet morphology. *Phys. Fluids* **28** (3), 033305.

Bajpai, A., Bhateja, A. & Kumar, R. 2024 Plume-surface interaction during lunar landing using a two-way coupled DSMC-DEM approach. *Phys. Rev. Fluids* **9** (2), 024306.

Barenblatt, G.I., Chorin, A.J. & Prostokishin, V.M. 2005 The turbulent wall jet: a triple-layered structure and incomplete similarity. *Proc. Natl Acad. Sci.* **102** (25), 8850–8853.

Benseghier, Z., Luu, L.H., Cuéllar, P., Bonelli, S. & Philippe, P. 2023 On the erosion of cohesive granular soils by a submerged jet: a numerical approach. *Granul. Matt.* **25** (1), 8.

Clark, A.H. & Behringer, R.P. 2014 Jet-induced 2-D crater formation with horizontal symmetry breaking. *Granul. Matt.* **16** (4), 433–440.

Croft, S.K. 1985 The scaling of complex craters. *J. Geophys. Res.* **90** (S02), C828–C842.

Cushman-Roisin, B. 2014 Turbulent jets. In *Environmental Fluid Mechanics*, pp. 153–161. John Wiley & Sons.

Donohue, C.M., Metzger, P.T. & Immer, C.D. 2021 Empirical scaling laws of rocket exhaust cratering. arXiv:2104.05176.

Gong, M., Azadi, S., Gans, A., Gondret, P. & Sauret, A. 2021 Erosion of a cohesive granular material by an impinging turbulent jet. In *EPJ Web of Conferences*, vol. 249, p. 08011. EDP Sciences.

Gorman, M.T., Rubio, J.S., Diaz-Lopez, M.X., Chambers, W.A., Korzun, A.M., Rabinovitch, J. & Ni, R. 2023 Scaling laws of plume-induced granular cratering. *PNAS Nexus* **2** (9), pgad300.

Guleria, S.D. & Patil, D.V. 2020 Experimental investigations of crater formation on granular bed subjected to an air-jet impingement. *Phys. Fluids* **32** (5), 053309.

Holsapple, K.A. & Schmidt, R.M. 1982 On the scaling of crater dimensions. 2. Impact processes. *J. Geophys. Res.* **87** (B3), 1849–1870.

Katsuragi, H. 2010 Morphology scaling of drop impact onto a granular layer. *Phys. Rev. Lett.* **104** (21), 218001.

Katsuragi, H. 2016 *Physics of Soft Impact and Cratering*, 1st edn. Lecture Notes in Physics, vol. 910. Springer.

Kuang, S.B., LaMarche, C.Q., Curtis, J.S. & Yu, A.B. 2013 Discrete particle simulation of jet-induced cratering of a granular bed. *Powder Technol.* **239**, 319–336.

LaMarche, C.Q. & Curtis, J.S. 2015 Cratering of a particle bed by a subsonic turbulent jet: effect of particle shape, size and density. *Chem. Engng Sci.* **138**, 432–445.

Lane, J.E., Metzger, P.T., Clements, S. & Immer, C.D. 2010 Cratering and blowing soil by rocket engines during lunar landings. In *Lunar Settlements*, pp. 569–594. CRC Press.

Launder, B.E. & Rodi, W. 1979 The turbulent wall jet. *Prog. Aerosp. Sci.* **19**, 81–128.

Launder, B.E. & Rodi, W. 1983 The turbulent wall jet measurements and modeling. *Annu. Rev. Fluid Mech.* **15** (1), 429–459.

Lohse, D., Bergmann, R., Mikkelsen, R., Zeilstra, C., Van Der Meer, D., Versluis, M., Van Der Weele, K., van der Hoef, M. & Kuipers, H. 2004 Impact on soft sand: void collapse and jet formation. *Phys. Rev. Lett.* **93** (19), 198003.

MARUOKA, H. 2023 A framework for crossover of scaling law as a self-similar solution: dynamical impact of viscoelastic board. *Eur. Phys. J.* E **46** (5), 35.

METZGER, P.T. 2024*a* Erosion rate of lunar soil under a landing rocket. Part 1. Identifying the rate-limiting physics. *Icarus* **417**, 116136.

METZGER, P.T. 2024*b* Erosion rate of lunar soil under a landing rocket. Part 2. Benchmarking and predictions. *Icarus* **417**, 116135.

METZGER, P.T., LATTA III, R.C., SCHULER, J.M. & IMMER, C.D. 2009 Craters formed in granular beds by impinging jets of gas. In *AIP Conference Proceedings*, vol. 1145, pp. 767–770. American Institute of Physics.

METZGER, P.T., SMITH, J. & LANE, J.E. 2011 Phenomenology of soil erosion due to rocket exhaust on the Moon and the Mauna Kea lunar test site. *J. Geophys. Res.* **116**, E06005.

NEFZAOUI, E. & SKURTYS, O. 2012 Impact of a liquid drop on a granular medium: inertia, viscosity and surface tension effects on the drop deformation. *Expl Therm. Fluid Sci.* **41**, 43–50.

PRIEUR, N.C., ROLF, T., LUTHER, R., WÜNNEMANN, K., XIAO, Z. & WERNER, S.C. 2017 The effect of target properties on transient crater scaling for simple craters. *J. Geophys. Res.* **122** (8), 1704–1726.

RAJARATNAM, N. & BELTAOS, S. 1977 Erosion by impinging circular turbulent jets. *J. Hydraul. Div. ASCE* **103** (10), 1191–1205.

SCHLICHTING, H. & GERSTEN, K. 1979 *Boundary-Layer Theory*, 7th edn. McGraw-Hill.

SCOTT, R.F. & KO, H.Y. 1968 Transient rocket-engine gas flow in soil. *AIAA J.* **6** (2), 258–264.

TOIGO, A.D. & RICHARDSON, M.I. 2003 Meteorology of proposed Mars Exploration Rover landing sites. *J. Geophys. Res.* **108** (E12).

UEHARA, J.S., AMBROSO, M.A., OJHA, R.P. & DURIAN, D.J. 2003 Low-speed impact craters in loose granular media. *Phys. Rev. Lett.* **90** (19), 194301.

VAN DER MEER, D. 2017 Impact on granular beds. *Annu. Rev. Fluid Mech.* **49**, 463–484.

WITZE, A. 2023 Moon mission failure: why is it so hard to pull off a lunar landing? *Nature* https://doi.org/10.1038/d41586-023-01454-7.

YAMAMOTO, S., HASEGAWA, S., SUZUKI, A.I. & MATSUNAGA, T. 2017 Impact velocity dependence of transient cratering growth. *J. Geophys. Res.* **122** (5), 1077–1089.

YUE, Z. 2001 Air jets in ventilation applications. *Build. Serv. Engng R. Inst. Technol. Bull.* (55).

ZHAO, R., ZHANG, Q., TJUGITO, H. & CHENG, X. 2015*a* Granular impact cratering by liquid drops: understanding raindrop imprints through an analogy to asteroid strikes. *Proc. Natl Acad. Sci.* **112** (2), 342–347.

ZHAO, S.C., DE JONG, R. & VAN DER MEER, D. 2015*b* Raindrop impact on sand: a dynamic explanation of crater morphologies. *Soft Matt.* **11** (33), 6562–6568.

ZHAO, S.C., DE JONG, R. & VAN DER MEER, D. 2017 Liquid-grain mixing suppresses droplet spreading and splashing during impact. *Phys. Rev. Lett.* **118** (5), 054502.

ZHAO, Z., ZHAO, J. & LIU, H. 2013 Landing dynamic and key parameter estimations of a landing mechanism to asteroid with soft surface. *Intl J. Aeronaut. Space Sci.* **14** (3), 237–246.